UC San Diego
UC San Diego Previously Published Works

Title

Nanobody-Facilitated Multiparametric PET/MRI Phenotyping of Atherosclerosis

Permalink

Journal

JACC Cardiovascular Imaging, 12(10)

ISSN

Authors

Senders, Max L
Hernot, Sophie
Carlucci, Giuseppe
et al.

Publication Date

2019-10-01

DOI

Peer reviewed

Nanobody-Facilitated Multiparametric PET/MRI Phenotyping of Atherosclerosis

Max L. Senders, MD[a,b], **Sophie Hernot, PHD**[c], **Giuseppe Carlucci, PHD**[d,e], **Jan C. van de Voort, BS**[a], **Francois Fay, PHD**[a,f], **Claudia Calcagno, MD, PHD**[a], **Jun Tang, PHD**[e], **Amr Alaarg, PHD**[a,g], **Yiming Zhao, PHD**[a], **Seigo Ishino, PHD**[a], **Anna Palmisano, MD**[a,h], **Gilles Boeykens, BS**[a], **Anu E. Meerwaldt, MS**[a], **Brenda L. Sanchez-Gaytan, PHD**[a], **Samantha Baxter, MHS**[a], **Laura Zendman, MS**[a], **Mark E. Lobatto, MD, PHD**[i], **Nicolas A. Karakatsanis, PHD**[a], **Philip M. Robson, PHD**[a], **Alexis Broisat, PHD**[j], **Geert Raes, PHD**[k,l], **Jason S. Lewis, PHD**[e,m,n], **Sotirios Tsimikas, MD**[o], **Thomas Reiner, PHD**[e,m], **Zahi A. Fayad, PHD**[a], **Nick Devoogdt, PHD**[c], **Willem J.M. Mulder, PHD**[a,b], **Carlos Pérez-Medina, PHD**[a]

[a]Translational and Molecular Imaging Institute, Icahn School of Medicine at Mount Sinai, New York, New York; [b]Department of Medical Biochemistry, Academic Medical Center, Amsterdam, the Netherlands; [c]In Vivo Cellular and Molecular Imaging Laboratory, Vrije Universiteit Brussel, Brussels, Belgium; [d]Bernard and Irene Schwarz Center for Biomedical Imaging, New York University, New York, New York; [e]Department of Radiology, Memorial Sloan-Kettering Cancer Center, New York, New York; [f]Department of Chemistry, York College of The City University of New York, New York, New York; [g]Department of Biomaterials Science and Technology, Technical Medical Centre. University of Twente, Enschede, the Netherlands; [h]Unit of Clinical Research in Radiology, Experimental Imaging Center, San Raffaele Scientific Institute, Milan, Italy; [i]Department of Radiology, Academic Medical Center, Amsterdam, the Netherlands; [j]Bioclinic Radiopharmaceutics Laboratory, Institut National de la Santé et de la Recherche Médicale Unité Mixte de Recherche S 1039, Grenoble, France; [k]Research Group of Cellular and Molecular Immunology, Vrije Universiteit Brussel, Brussels, Belgium; [l]Laboratory of Myeloid Cell Immunology, Vlaams Instituut voor Biotechnologie Inflammation Research Center, Ghent, Belgium; [m]Department of Radiology, Weill Cornell Medical College, New York, New York; [n]Molecular Pharmacology Program, Memorial Sloan Kettering Cancer Center, New York, New York; [o]Division of Cardiovascular Diseases, Sulpizio Cardiovascular Center, Department of Medicine, University of California, La Jolla, San Diego, California.

Abstract

OBJECTIVES—This study sought to develop an integrative positron emission tomography (PET) with magnetic resonance imaging (MRI) procedure for accurate atherosclerotic plaque phenotyping, facilitated by clinically approved and nanobody radiotracers.

ADDRESS FOR CORRESPONDENCE: Dr. Carlos Pérez-Medina, Translational and Molecular Imaging Institute, Icahn School of Medicine at Mount Sinai, 1470 Madison Avenue, New York, New York 10029. carlos.perez-medina@mountsinai.org. OR Dr. Willem J.M. Mulder, Translational and Molecular Imaging Institute, Icahn School of Medicine at Mount Sinai, One Gustave L. Levy Place, Box 1234, New York, New York 10029. willem.mulder@mssm.edu.

APPENDIX For supplemental material including tables and figures, please see the online version of this paper.

BACKGROUND—Noninvasive characterization of atherosclerosis remains a challenge in clinical practice. The limitations of current diagnostic methods demonstrate that, in addition to atherosclerotic plaque morphology and composition, disease activity needs to be evaluated.

METHODS—We screened 3 nanobody radiotracers targeted to different biomarkers of atherosclerosis progression, namely vascular cell adhesion molecule (VCAM)-1, lectin-like oxidized low-density lipoprotein receptor (LOX)-1, and macrophage mannose receptor (MMR). The nanobodies, initially radiolabeled with copper-64 (^{64}Cu), were extensively evaluated in *Apoe*$^{-/-}$ mice and atherosclerotic rabbits using a combination of in vivo PET/MRI readouts and ex vivo radioactivity counting, autoradiography, and histological analyses.

RESULTS—The 3 nanobody radiotracers accumulated in atherosclerotic plaques and displayed short circulation times due to fast renal clearance. The MMR nanobody was selected for labeling with gallium-68 (^{68}Ga), a short-lived radioisotope with high clinical relevance, and used in an ensuing atherosclerosis progression PET/MRI study. Macrophage burden was longitudinally studied by ^{68}Ga-MMR–PET, plaque burden by T2-weighted MRI, and neovascularization by dynamic contrast-enhanced (DCE) MRI. Additionally, inflammation and microcalcifications were evaluated by fluorine-18 (^{18}F)-labeled fluorodeoxyglucose (^{18}F-FDG) and ^{18}F-sodium fluoride (^{18}F-NaF) PET, respectively. We observed an increase in all the aforementioned measures as disease progressed, and the imaging signatures correlated with histopathological features.

CONCLUSIONS—We have evaluated nanobody-based radiotracers in rabbits and developed an integrative PET/MRI protocol that allows noninvasive assessment of different processes relevant to atherosclerosis progression. This approach allows the multiparametric study of atherosclerosis and can aid in early stage anti-atherosclerosis drug trials.

Keywords

atherosclerosis; molecular imaging; nanobody; PET/MRI

Atherosclerosis is an inflammatory disorder of the major arteries that is causative of cardiovascular disease (1). Lipid-driven progression of inflamed atherosclerotic lesions, initiated by vascular endothelium disruption, causes their development into plaques. In the process, inflammatory monocytes are recruited, which subsequently differentiate into macrophages that proliferate and evolve into foam cells (2,3). Further progression is characterized by calcium depositions and additional lipid accumulation, resulting in plaque expansion with hypoxia-induced neovascularization (4). Eventually, acute cardiovascular events like myocardial infarction and stroke may occur as a result of plaque erosion or rupture. Unfortunately, myocardial infarction and sudden cardiac death are frequently the first signs of cardiovascular disease in patients with otherwise a risk factor—free profile (5).

The limitations of current diagnostic methods demonstrate that, in addition to plaque morphology and composition, disease activity needs to be evaluated (6). Over the past 2 decades, many different imaging approaches have been proposed to study the pathophysiological processes associated with atherosclerosis progression (7). Positron emission tomography (PET) imaging with fluorine-18 (^{18}F)-labeled fluorodeoxyglucose (^{18}F-FDG), for instance, is a clinically viable method to noninvasively quantify plaque inflammation (8,9). However, ^{18}F-FDG lacks specificity as it is taken up by metabolically

active cells, rendering imaging of the coronary arteries particularly challenging due to avid myocardial up-take (10). More recently, ^{18}F-sodium fluoride (^{18}FNaF) PET has emerged as a promising method to visualize plaque microcalcifications (11). Yet, due to the inherent limitations of standalone molecular imaging techniques, precise phenotyping of athero-sclerotic lesions would profoundly benefit from an integrative multimodal imaging approach allowing simultaneous quantification of different key disease progression features. This would not only have a potential impact on future anti-atherosclerosis drug clinical drug trials (9), but it is immediately relevant on a pre-clinical level, both for a better understanding of atherosclerosis biology and the development and evaluation of new drugs, noninvasively and longitudinally in animals.

The advent of fully integrated PET/magnetic resonance imaging (MRI) scanners brings together the strengths of the individual imaging modalities, that is, MRI's excellent soft tissue contrast and real 3-dimensional imaging capabilities, and PET's sensitivity and radiotracer specificity. This synergy can be exploited advantageously for vessel wall imaging, as it allows accurate delineation of lesions and coregistration of functional information derived from the radiotracer's PET signal. In addition, MRI functional methods can be integrated to assess vessel wall permeability, as a measure of plaque neovascularization (12), and may be combined with vessel wall morphological assessment (13).

Here, we integrated nanobody radiotracer technology in a multiparametric PET/MRI protocol that allows precise characterization of the atherosclerotic plaque. Antibodies have been extensively used as PET/single-photon emission computed tomography radiotracers, although long blood circulation times prohibit their use for vessel wall imaging. In contrast, nanobody-based radiotracers are extremely well suited for this purpose, as their high affinity and specificity are similar to antibodies (14), but their markedly smaller size facilitates rapid blood clearance (Figure 1A). Capitalizing on established work (15–17), we selected 3 nanobodies specific to different clinically relevant key markers of atherosclerosis progression (18), namely vascular cell adhesion molecule (VCAM)-1 (19), lectin-like oxidized low-density lipoprotein receptor-1 (LOX-1) (20), and macrophage mannose receptor (MMR) (21) (Figure 1B). These nanobodies, labeled with copper-64 (^{64}Cu), were first extensively screened in *Apoe*$^{-/-}$ mice and atherosclerotic rabbits (Figure 1C).

Finally, the MMR nanobody was further developed into a gallium-68 (^{68}Ga)-labeled PET tracer. This tracer was then integrated in a multimodal protocol on a clinical PET/MRI system to simultaneously study vessel wall morphology and atherosclerotic plaque activity. The imaging protocol, involving ^{68}Ga-MMR nanobody-PET, anatomical and dynamic contrast enhanced (DCE) MRI, in addition to ^{18}F-FDG-PET and ^{18}F-NaF-PET, was applied to study atherosclerosis progression in rabbits (Figure 1C).

METHODS

A complete description of the methods is provided in the Online Appendix. All animal experiments were performed in accordance with protocols approved by the Institutional

Animal Care and Use Committees of Mount Sinai and/or Memorial Sloan Kettering Cancer Center and followed National Institutes of Health guidelines for animal welfare.

RESULTS

NANOBODY-RADIOTRACER SCREENING IN MICE.

Nanobodies targeting 3 relevant markers of atherosclerosis progression (15–17) were screened for use in molecular imaging of atherosclerosis. A nanobody targeting myeloma protein was used as chemical control. The nanobodies were functionalized with the chelator 1,4,7-triazacyclononane-1,4,7-triacetic acid (NOTA). This modification was well tolerated, as the target affinity was retained (Online Table 1). The nanobodies were radiolabeled with ^{64}Cu for preliminary in vivo screening in *Apoe*$^{-/-}$ mice, as this radioisotope allows extensive ex vivo evaluation due to its 12.7-h decay half-life. Radiolabeling of all nanobodies proceeded in high radiochemical yield and purity (Figure 1D). Biodistribution in *Apoe*$^{-/-}$ mice at 3 h post-injection (p.i.) revealed high kidney up-take for all nanobodies, but with varying organ/tissue distribution patterns (Figure 2A, Online Table 2). Moreover, all nanobodies showed rapid blood radioactivity clearance with blood half-lives shorter than 2 min (Online Figure 1). Autoradiography revealed preferential ^{64}Cu deposition at typical lesion sites such as the aortic root for all radiotracers, whereas the control nanobody showed a homogeneous distribution pattern (Figure 2B). Whole-aorta radioactivity concentration was highest for ^{64}Cu-MMR, as was the aorta-to-blood ratio (Figure 2C). We selected ^{64}Cu-MMR and ^{64}Cu-VCAM for additional micro–PET/computed tomography imaging, showing significant radioactivity accumulation in the aortic root and arch, where advanced lesions typically develop (Figure 2D). Strong kidney and bladder signals were observed, indicative of fast renal clearance. Radiotracer cellular specificity in the plaque was assessed in sections taken from the aortic root of mice injected with the radiolabeled nanobodies. Autoradiography of aortic sections showed colocalization of radioactivity with the expected cell types for each nanobody, that is, endothelial cells for ^{64}Cu-VCAM, macrophages for ^{64}Cu-MMR, and both for ^{64}Cu-LOX, and immunofluorescence confirmed target specificity for all nanobodies (15–17) (Figure 2E).

PET/MRI PLAQUE PHENOTYPING OF RABBIT ATHEROSCLEROTIC AORTAS.

In vivo imaging experiments were conducted for the 3 ^{64}Cu-labeled nanobodies in a rabbit model of atherosclerosis using a clinical PET/MRI scanner (Online Figure 2). A comprehensive in vivo PET/MRI analysis of atherosclerotic aortas of rabbits injected with the ^{64}Cu-nanobodies was carried out. In addition to nanobody PET, the multimodal imaging protocol also included T2-weighted–MRI measurement of vessel wall area (Figure 3A, left) and DCE-MRI–based evaluation of vascular permeability (Figure 3A, right). Additionally, an ^{18}F-FDG-PET scan was performed 2 days before the nanobody-PET scan to allow direct comparison between ^{18}F-FDG and the nanobody radiotracers in the same rabbit (Figure 3B, left). Representative PET/MR fusion images of aortas from rabbits injected with the ^{64}Cu-nanobodies recorded between 160 and 170 min p.i. are shown in Figure 3B (right). T2-weighted–based plaque area, DCE-MRI measurements, and ^{18}F-FDG uptake were similar among the 3 groups of rabbits. Overall, these parameters suggest a similar degree of disease burden for all groups. Similar to the mouse studies, we found fast blood clearance with

varying organ distributions by ex vivo gamma counting (Online Figures 3A and 3B). Radioactivity concentration in the aorta and aorta-to-muscle, aorta-to-blood, and aorta-to-lung ratios were comparable for all nanobody radiotracers, whereas aorta-to-heart and aorta-to-liver ratios showed significant differences (Online Figure 3C). In concordance with mouse findings, autoradiography of abdominal rabbit aortas showed a heterogeneous radioactivity distribution pattern for ^{64}Cu-VCAM and, especially, ^{64}Cu-MMR (Online Figure 3D). The evaluation of a radiotracer's potential to discriminate atherosclerotic lesions from healthy segments in the vessel wall should take into account the disease's heterogeneity. Aorta-to-blood ratios are based on aortic value averages from healthy and diseased segments. To better appreciate the nanobody tracers' atherosclerosis imaging potential, we conducted a careful autoradiographic analysis (Online Figure 4A). The most diseased segments (MDS) had about 1.5×,3×, and 4× more counts per unit area than the corresponding atherosclerosis-free, least diseased segments for ^{64}Cu-LOX, ^{64}Cu-VCAM, and ^{64}Cu-MMR, respectively (Online Figures 4B and 4C). Moreover, MDS for ^{64}Cu-MMR contained more than 2× the radioactivity per unit area than the average whole abdominal aorta (Online Figure 4D). For illustrative purposes, we also computed MDS-to-blood and MDS-to-heart ratios (Online Figures 4E and 4F). Collectively, these data suggest that the MMR nanobody has a high atherosclerosis imaging potential. A summary of the key findings from the ^{64}Cu-nanobody tracer studies in mice and rabbits can be found in Table 1.

To investigate whether nanobody tracer accumulation was related to plaque size, inflammation, or permeability, we performed extensive comparative region-by-region analyses between their uptake and the different parameters evaluated by our multi-pronged imaging protocol (Online Figure 5). Interestingly, aortic ^{64}Cu-MMR uptake was not significantly correlated with the uptake of ^{18}F-FDG, but ^{64}Cu-MMR uptake did show a positive correlation with vessel wall area (Online Figure 5A). We also found a significant inverse correlation between ^{64}Cu-VCAM uptake and vessel wall area. Ex vivo radioactivity distribution in the aorta was evaluated by digital autoradiography and compared against the other parameters using a similar analysis (Online Figure 6A). Importantly, significant correlations were found between PET-derived standardized uptake values and radioactivity deposition as quantified from the autoradiographs for all ^{64}Cu-nanobodies, demonstrating the reliability of the imaging-derived values (Online Figure 6B). No correlation was found between any ^{64}Cu-nanobody uptake and vascular permeability, as measured by DCE-MRI, suggesting that their accumulation in the vessel wall is not governed by this parameter (Online Figure 6C).

PET/MRI EVALUATION OF ATHEROSCLEROSIS PROGRESSION.

Due to its favorable pharmacokinetics and plaque macrophage specificity, the MMR nanobody was further included in a PET/MRI atherosclerosis progression study. To match the nanobody's short blood circulation time and pursue a translational approach, in the ensuing experiments we used the shorter-lived isotope ^{68}Ga (physical half-life = 68 min). We obtained ^{68}Ga-MMR in high radiochemical yield and purity. Importantly, no meaningful differences were found between the ^{68}Ga-labeled VCAM and MMR nanobodies and their ^{64}Cu-labeled counterparts in preliminary experiments carried out in *Apoe*$^{-/-}$ mice (Online Figure 7).

The study also included static ^{18}F-FDG and ^{18}F-NaF PET scans on consecutive days before the multi-parametric 68Ga-MMR PET/MRI session (Online Figure 8A). We observed a gradual increase in ^{18}F-FDG and ^{68}Ga-MMR PET signal intensities in the aorta as disease progressed (Figure 4A). Interestingly, although ^{18}F-NaF PET aortic signal was similar between control subjects and rabbits fed a cholesterol-enriched high-fat diet (HFD) for 4 months, a significant increase after 8 months on HFD was found. Aorta-to-muscle ratios showed a similar trend (Online Figure 8B). Finally, vessel wall area and permeability also increased as disease advanced (Figure 4B). Online Table 3 summarizes the main imaging parameters for the 3 tracers.

To explore the feasibility of coronary imaging, cardiac uptake for the 3 radiotracers was determined by PET to calculate the aorta-to-heart ratios in rabbits with advanced atherosclerosis (8-month HFD) (Figure 4C). The PET scan showed that ^{18}F-NaF had the highest ratio due to its low uptake in cardiac tissue, followed by ^{68}Ga-MMR and ^{18}F-FDG, whose uptake in the myocardium was relatively high (standardized uptake value 2 to 4 g/ml) despite a 4-h fasting protocol before injection. Similar to ^{64}Cu-MMR results, vessel wall area was significantly associated with 68Ga-MMR uptake (r = 0.55, p = 0.0002), which is indicative of macrophage accumulation in atherosclerosis progression. The ^{68}Ga-MMR PET images were dominated by a strong kidney signal in all groups, and no significant differences were found in organ uptake for all tracers (kidney, liver, bone marrow—or bone for ^{18}F-NaF—and spleen) among the 3 groups (Online Figure 8C). Ex vivo quantification of aortic uptake by gamma counting corroborated the in vivo findings (Online Figure 8D, left). Marked differences in radioactivity deposition patterns were also observed between control and atherosclerosis groups by autoradiography (Online Figure 8D, right). Of note, the blood half-life for ^{68}Ga-MMR was similar in all 3 groups (Online Figure 8E).

Histological evaluation of aortic sections confirmed disease progression as shown by increased plaque area and macrophage content (Figure 4D), as well as microcalcifications (Online Figure 9A), in atherosclerotic aortas and absence of these hallmarks in the control and 4-month HFD groups. Quantitative analysis revealed a significant increase in plaque size, macrophage content, and MMR (CD206) expression as disease progressed (Figures 5A and 5B). Importantly, CD206 immunostaining of diseased aortas correlated significantly with ^{68}Ga-MMR radioactivity measured by autoradiography (Figure 5C). We found no CD206 staining in the control group, whereas expression was observed in both atherosclerotic rabbit groups (Figure 5A and Online Figure 9A). Of note, a significant correlation between macrophage content and our nanobody tracer was found in 4-month HFD rabbits, whereas in 8-month HFD rabbits the correlation weakened (Online Figure 9B).

In summary, using this multiparametric imaging protocol, we were able to quantify different hallmarks of atherosclerosis in a noninvasive fashion. The observed imaging results were corroborated ex vivo by different techniques, demonstrating the robustness of this imaging approach to longitudinally evaluate disease burden.

DISCUSSION

Three nanobodies targeting 3 well-established markers related to monocyte/macrophage dynamics were screened to identify key features of atherosclerotic lesions. In contrast to long-circulating full-size antibodies (22), the use of radiolabeled nanobodies enables PET vessel wall imaging at earlier time points due to their rapid blood clearance after injection. Conveniently, nanobodies' shorter circulation times allow their labeling with short-lived isotopes, substantially reducing radiation exposure. Indeed, in vivo PET/MRI biodistribution evaluation showed fast radioactivity clearance from blood that was mirrored by a rapid accumulation in the kidneys, confirming renal clearance for all nanobody tracers. Similar biodistribution patterns were observed in mice and rabbits. However, whereas in rabbits there was no clear difference among aortic ^{64}Cu-nanobody up-takes, in $Apoe^{-/-}$ mice ^{64}Cu-MMR uptake was significantly higher. Although this uptake can be attributed in part to MMR-positive cells in the adventitial layer and the surrounding perivascular tissue of atherosclerotic lesions of $Apoe^{-/-}$ mice (23), in rabbits we did observe an increased plaque up-take compared to control subjects and expression of the mannose receptor within the lesions. These observations likely reflect the differences in lesion composition between the 2 models (24).

Using our newly developed multiparametric atherosclerosis imaging protocol, we noninvasively observed a similar disease burden in all rabbits. Comparative analyses revealed a moderate correlation between vessel wall area and permeability, pointing to a certain degree of association between lesion size and neovascularization. Interestingly, whereas ^{64}Cu-VCAM uptake did not correlate with DCE-MRI permeability measurements, its uptake was negatively associated with vessel wall area, both in vivo and ex vivo. These findings are consistent with the distinct expression of VCAM-1 in early atherosclerotic lesions (25) and may warrant further research into the use of this VCAM-1 nanobody radiotracer to detect such lesions. The MMR nanobody tracer was further included in an atherosclerosis progression study. To enhance translatability, and to match its short blood circulation half-life, we labeled the MMR nanobody with the clinically relevant (26), short-lived isotope ^{68}Ga. This facilitated a unique head-to-head comparison between clinically available radiotracers, namely ^{18}F-FDG and ^{18}F-NaF, and the MMR nanobody radiotracer. Image analysis revealed a significantly higher aortic uptake for ^{18}F-FDG, ^{18}F-NaF, and ^{68}Ga-MMR in rabbits with advanced atherosclerotic lesions as compared to healthy control subjects, which is indicative of increased vessel wall inflammatory activity, microcalcification, and macrophage burden, respectively. MR-based measurements also revealed an increase in vessel wall area and permeability. These findings are consistent with an increased plaque burden, although the 3 radio-tracers seemed to accumulate at different locations and/or concentrations throughout the aorta as evidenced by the absence of significant correlations between their respective uptakes. This is in keeping with previous studies reporting a low degree of colocalization between ^{18}F-FDG and ^{18}F-NaF in atherosclerotic lesions (27). Moreover, our histological and autoradiographic analyses of aortic sections showed no significant association between macrophage burden and mineral deposits. Taken together, these data are consistent with a temporal separation between the processes imaged by the 2 tracers, because macrophage-mediated inflammation and mineral

deposition are considered hallmarks of early and advanced lesions, respectively. Therefore, these 2 tracers seem complementary and their combined use as a "cocktail" (28) could be of value also in atherosclerosis.

The mannose receptor (*MRC1*, CD206) has been historically used as a marker for alternatively activated macrophages (29,30). Its expression has been shown in human lesions with intraplaque hemorrhage and in thin cap fibroatheromas (31,32), making it a potential marker of plaque vulnerability. Over the last decades, ^{18}F-FDG has been exploited as a surrogate PET radiotracer for plaque inflammation. Although ^{18}F-FDG is mainly taken up by macrophages (8), other processes than inflammation and other cell types may also contribute to its accumulation in atherosclerotic plaques (33). Moreover, alternatively activated and inflammatory macrophages have been shown to utilize glucose to a similar extent (34). In this study, we found a weak correlation between ^{18}F-FDG and ^{64}Cu-MMR uptake measured ex vivo, whereas no relationship was found between ^{64}Cu-MMR and HDL uptake, which was used to map macrophages by near infrared fluorescence (NIRF) imaging (35) and did correlate with ^{18}F-FDG uptake. Collectively, these data indicate that different macrophage populations are targeted by these 2 radiotracers, that is, all versus CD206^{+} macrophages. Ensuing studies will have to elucidate the complex relationships among inflammation, macrophage phenotype, glucose metabolism, and ^{18}F-FDG uptake in the vessel wall.

One of the limitations of atherosclerosis imaging with ^{18}F-FDG is the elevated myocardial uptake, which hinders accurate identification of lesions in the coronary arteries (36). For comparative purposes, PET-derived aorta-to-heart uptake ratios in diseased rabbits were calculated for ^{18}F-FDG, ^{18}FNaF, and ^{68}Ga-MMR as a measure of their ability to image atherosclerosis in the coronary arteries. Although the MMR nanobody did not show as high a background signal as ^{18}F-FDG, its moderate aorta-to-heart uptake ratio—probably due to the presence of "background" cardiac resident macrophages (37)—may limit its ability to image coronary plaques to areas with significant macrophage burden. In this respect, ^{18}F-NaF has an enormous advantage, as its cardiac uptake is low. However, in this rabbit model, we had to exclude some aortic regions from our analysis due to elevated ^{18}F-NaF uptake in nearby vertebrae. In the future, this might prevent reliable aortic imaging in patients, whereas ^{18}F-FDG and ^{68}Ga-MMR showed lower uptake in the vertebrae aside from a marginal uptake in the bone marrow.

In recent years, the community has witnessed a shift in atherosclerosis research toward an integral disease and away from the individual culprit plaque. Monocyte recruitment and local macrophage proliferation have been identified as key processes in atherosclerotic progression, and recent insights indicate some degree of neural involvement (38). Characterizing all these processes in a longitudinal fashion would enormously benefit from a noninvasive imaging approach. PET is intrinsically a "hot spot" technique and therefore particularly suited to study biological processes systemically (38). From a clinical perspective, noninvasive imaging has already been successfully used to provide surrogate endpoints in clinical trials (9). These often require a large number of participants to ensure a meaningful level of statistical significance is achieved, with long follow-up periods, as the primary endpoint is typically mortality. Robust noninvasive readouts are therefore extremely

beneficial as they directly probe treatment response and thereby provide reliable information in a much shorter time frame. In this setting, an imaging approach like the one described here can be of great value. Furthermore, the protocol could be additionally complemented by incorporation of noncontrast T1-weighted MRI to investigate the presence of intraplaque hemorrhage or thrombus (39,40), whereas quantitative evaluation of the fibrous cap and the lipid-rich necrotic core could be performed by T2-weighted MRI (41). Thus, several specific aspects of the disease can be interrogated simultaneously to obtain a more complete representation of the intervention outcome.

CONCLUSIONS

We have translated nanobody-based radiotracer technology to rabbits for the first time and integrated it in a PET/MRI protocol that allows evaluation of several key features of atherosclerosis progression. Our protocol enabled reliable phenotyping of rabbit atherosclerotic lesions over time, as well as extensive comparison of the nanobody probes with different clinical radiotracers. Here, we advocate this multi-parametric imaging approach that may be used to aid in early stage drug development as well as in identification of high-risk patients. We believe that the nanobody tracers presented in this study complement the clinically available tracers ^{18}F-FDG and ^{18}F-NaF and, as attested by the phase I clinical trial of a HER2 nanobody tracer to identify patients with breast cancer (26), their translation is within reach.

Supplementary Material

Refer to Web version on PubMed Central for supplementary material.

Acknowledgments

ABBREVIATIONS AND ACRONYMS

[64]Cu	copper-64
DCE	dynamic contrast-enhanced
^{18}F-FDG	^{18}F-fluorodeoxyglucose
[18]F-NaF	^{18}F-sodium fluoride
[68]Ga	gallium-68
HFD	high-fat diet

LOX	lectin-like oxidized low-density lipoprotein receptor
MDS	most diseased segment
MMR	macrophage mannose receptor
MRI	magnetic resonance imaging
PET	positron emission tomography
p.i.	post-injection
VCAM	vascular cell adhesion molecule

REFERENCES

1. Hansson GK. Inflammation, atherosclerosis, and coronary artery disease. N Engl J Med 2005;352: 1685–95. [PubMed: 15843671]

2. Robbins CS, Hilgendorf I, Weber GF, et al. Local proliferation dominates lesional macrophage accumulation in atherosclerosis. Nat Med 2013;19: 1166–72. [PubMed: 23933982]

3. Tabas I, Bornfeldt KE. Macrophage phenotype and function in different stages of atherosclerosis. Circ Res 2016;118:653–67. [PubMed: 26892964]

4. Moreno PR, Purushothaman K-R, Sirol M, Levy AP, Fuster V. Neovascularization in human atherosclerosis. Circulation 2006;113:2245–52. [PubMed: 16684874]

5. Narula J, Garg P, Achenbach S, Motoyama S, Virmani R, Strauss HW. Arithmetic of vulnerable plaques for noninvasive imaging. Nat Clin Pract Cardiovasc Med 2008;5:S2–10. [PubMed: 18641603]

6. Dweck MR, Aikawa E, Newby DE, et al. Noninvasive molecular imaging of disease activity in atherosclerosis. Circ Res 2016;119:330–40. [PubMed: 27390335]

7. Mulder WJ, Jaffer FA, Fayad ZA, Nahrendorf M. Imaging and nanomedicine in inflammatory atherosclerosis. Sci Transl Med 2014;6:239sr1. [PubMed: 24898749]

8. Tawakol A, Migrino RQ, Bashian GG, et al. In vivo 18F-fluorodeoxyglucose positron emission tomography imaging provides a noninvasive measure of carotid plaque inflammation in patients. J Am Coll Cardiol 2006;48:1818–24. [PubMed: 17084256]

9. Fayad ZA, Mani V, Woodward M, et al., for the dal-PLAQUE Investigators. Safety and efficacy of dalcetrapib on atherosclerotic disease using novel non-invasive multimodality imaging (dal-PLAQUE): a randomised clinical trial. Lancet 2011;378:1547–59. [PubMed: 21908036]

10. Joshi NV, Vesey AT, Williams MC, et al. 18F-fluoride positron emission tomography for identification of ruptured and high-risk coronary atherosclerotic plaques: a prospective clinical trial. Lancet 2014;383:705–13. [PubMed: 24224999]

11. Irkle A, Vesey AT, Lewis DY, et al. Identifying active vascular microcalcification by (18)F-sodium fluoride positron emission tomography. Nat Commun 2015;6:7495. [PubMed: 26151378]

12. Calcagno C, Lobatto ME, Dyvorne H, et al. Three-dimensional dynamic contrast-enhanced MRI for the accurate, extensive quantification of microvascular permeability in atherosclerotic plaques. NMR Biomed 2015;28:1304–14. [PubMed: 26332103]

13. Dweck MR, Williams MC, Moss AJ, Newby DE, Fayad ZA. Computed tomography and cardiac magnetic resonance in ischemic heart disease. J Am Coll Cardiol 2016;68:2201–16. [PubMed: 27855810]

14. Chakravarty R, Goel S, Cai W. Nanobody: the "magic bullet" for molecular imaging? Theranostics 2014;4:386–98. [PubMed: 24578722]

15. De Vos J, Mathijs I, Xavier C, et al. Specific targeting of atherosclerotic plaques in ApoE(−/−) mice using a new Camelid sdAb binding the vulnerable plaque marker LOX-1. Mol Imaging Biol 2014;16:690–8 [PubMed: 24687730]

16. Movahedi K, Schoonooghe S, Laoui D, et al. Nanobody-based targeting of the macrophage mannose receptor for effective in vivo imaging of tumor-associated macrophages. Cancer Res 2012; 72:4165–77. [PubMed: 22719068]

17. Broisat A, Hernot S, Toczek J, et al. Nano-bodies targeting mouse/human VCAM1 for the nuclear imaging of atherosclerotic lesions. Circ Res 2012;110:927–37. [PubMed: 22461363]

18. Falk E, Nakano M, Bentzon JF, Finn AV, Virmani R. Update on acute coronary syndromes: the pathologists' view. Eur Heart J 2013;34: 719–28. [PubMed: 23242196]

19. Mestas J, Ley K. Monocyte-endothelial cell interactions in the development of atherosclerosis. Trends Cardiovasc Med 2008;18:228–32. [PubMed: 19185814]

20. Mehta JL, Sanada N, Hu CP, et al. Deletion of LOX-1 reduces atherogenesis in LDLR knockout mice fed high cholesterol diet. Circ Res 2007;100: 1634–42. [PubMed: 17478727]

21. Gordon S Alternative activation of macrophages. Nat Rev Immunol 2003;3:23–35. [PubMed: 12511873]

22. Ishino S, Mukai T, Kuge Y, et al. Targeting of lectinlike oxidized low-density lipoprotein receptor 1 (LOX-1) with 99mTc-labeled anti-LOX-1 antibody: potential agent for imaging of vulnerable plaque. J Nucl Med 2008;49:1677–85. [PubMed: 18794262]

23. Bala G, Baudhuin H, Remory I, et al. Evaluation of [^{99m}Tc]radiolabeled macrophage mannose receptor-specific nanobodies for targeting of atherosclerotic lesions in mice. Mol Imaging Biol 2018;20:260–7. [PubMed: 28875290]

24. Getz GS, Reardon CA. Animal models of atherosclerosis. Arterioscler Thromb Vasc Biol 2012;32:1104–15. [PubMed: 22383700]

25. Iiyama K, Hajra L, Iiyama M, et al. Patterns of vascular cell adhesion molecule-1 and intercellular adhesion molecule-1 expression in rabbit and mouse atherosclerotic lesions and at sites predisposed to lesion formation. Circ Res 1999;85: 199–207. [PubMed: 10417402]

26. Keyaerts M, Xavier C, Heemskerk J, et al. Phase I study of 68Ga-HER2-nanobody for PET/CT assessment of HER2 expression in breast carcinoma. J Nucl Med 2016;57:27–33. [PubMed: 26449837]

27. Derlin T, Toth Z, Papp L, et al. Correlation of inflammation assessed by 18F-FDG PET, active mineral deposition assessed by 18F-fluoride PET, and vascular calcification in atherosclerotic plaque: a dual-tracer PET/CT study. J Nucl Med 2011; 52:1020–7. [PubMed: 21680686]

28. Iagaru A, Mittra E, Yaghoubi SS, et al. Novel strategy for a cocktail 18F-fluoride and 18F-FDG PET/CT scan for evaluation of malignancy: results of the pilot-phase study. J Nucl Med 2009;50: 501–5. [PubMed: 19289439]

29. Hirata Y, Tabata M, Kurobe H, et al. Coronary atherosclerosis is associated with macrophage polarization in epicardial adipose tissue. J Am Coll Cardiol 2011;58:248–55. [PubMed: 21737014]

30. Bourlier V, Zakaroff-Girard A, Miranville A, et al. Remodeling phenotype of human subcutaneous adipose tissue macrophages. Circulation 2008;117:806–15. [PubMed: 18227385]

31. Tahara N, Mukherjee J, de Haas HJ, et al. 2-deoxy-2-[18F]fluoro-D-mannose positron emission tomography imaging in atherosclerosis. Nat Med 2014;20:215–9. [PubMed: 24412923]

32. Finn AV, Nakano M, Polavarapu R, et al. Hemoglobin directs macrophage differentiation and prevents foam cell formation in human atherosclerotic plaques. J Am Coll Cardiol 2012;59:166–77. [PubMed: 22154776]

33. Folco EJ, Sheikine Y, Rocha VZ, et al. Hypoxia but not inflammation augments glucose uptake in human macrophages: implications for imaging atherosclerosis with 18fluorine-labeled 2-deoxy-D-glucose positron emission tomography. J Am Coll Cardiol 2011;58:603–14. [PubMed: 21798423]

34. Tavakoli S, Short JD, Downs K, et al. Differential regulation of macrophage glucose metabolism by macrophage colony-stimulating factor and granulocyte-macrophage colony-stimulating factor: implications for ^{18}F FDG PET imaging of vessel wall inflammation. Radiology 2016;283: 87–97. [PubMed: 27849433]

35. Pérez-Medina C, Binderup T, Lobatto ME, et al. In vivo PET imaging of HDL in multiple atherosclerosis models. J Am Coll Cardiol Img 2016;9: 950–61.

36. Rosenbaum D, Millon A, Fayad ZA. Molecular imaging in atherosclerosis: FDG PET. Curr Atheroscler Rep 2012;14:429–37. [PubMed: 22872371]

37. Majmudar MD, Yoo J, Keliher EJ, et al. Polymeric nanoparticle PET/MR imaging allows macrophage detection in atherosclerotic plaques. Circ Res 2013;112:755–61. [PubMed: 23300273]

38. Tawakol A, Ishai A, Takx RA, et al. Relation between resting amygdalar activity and cardiovascular events: a longitudinal and cohort study. Lancet 2017;389:834–45. [PubMed: 28088338]

39. Moody A, Allder S, Lennox G, Gladman J, Fentem P. Direct magnetic resonance imaging of carotid artery thrombus in acute stroke. Lancet 1999;353:122–3. [PubMed: 10023906]

40. Moody AR, Murphy RE, Morgan PS, et al. Characterization of complicated carotid plaque with magnetic resonance direct thrombus imaging in patients with cerebral ischemia. Circulation 2003;107:3047–52. [PubMed: 12796133]

41. Cai J, Hatsukami TS, Ferguson MS, et al. In vivo quantitative measurement of intact fibrous cap and lipid-rich necrotic core size in atherosclerotic carotid plaque: comparison of high-resolution, contrast-enhanced magnetic resonance imaging and histology. Circulation 2005;112:3437–44. [PubMed: 16301346]

PERSPECTIVES

COMPETENCY IN MEDICAL KNOWLEDGE:

Current diagnostic methods are very valuable in determining atherosclerotic plaque morphology and composition. However, whereas knowledge about the atherosclerosis disease process is growing, particularly related to inflammation's role, noninvasive imaging methods need to be developed. To this end, we combined target-specific nanobody-PET imaging information with functional and anatomical MRI readouts to develop an integrative multiparametric atherosclerotic plaque phenotyping procedure that reliably characterized lesions in an animal model of the disease.

TRANSLATIONAL OUTLOOK:

Our PET/MRI protocol has the potential to be translated to patients and, importantly, can be customized to include other clinically available tracers, such as ^{18}F-FDG or ^{18}F-NaF, or additional MRI-derived parameters. These imaging procedures may help to noninvasively unravel biological aspects of atherosclerosis and, ultimately, serve as a robust readout in clinical trials.
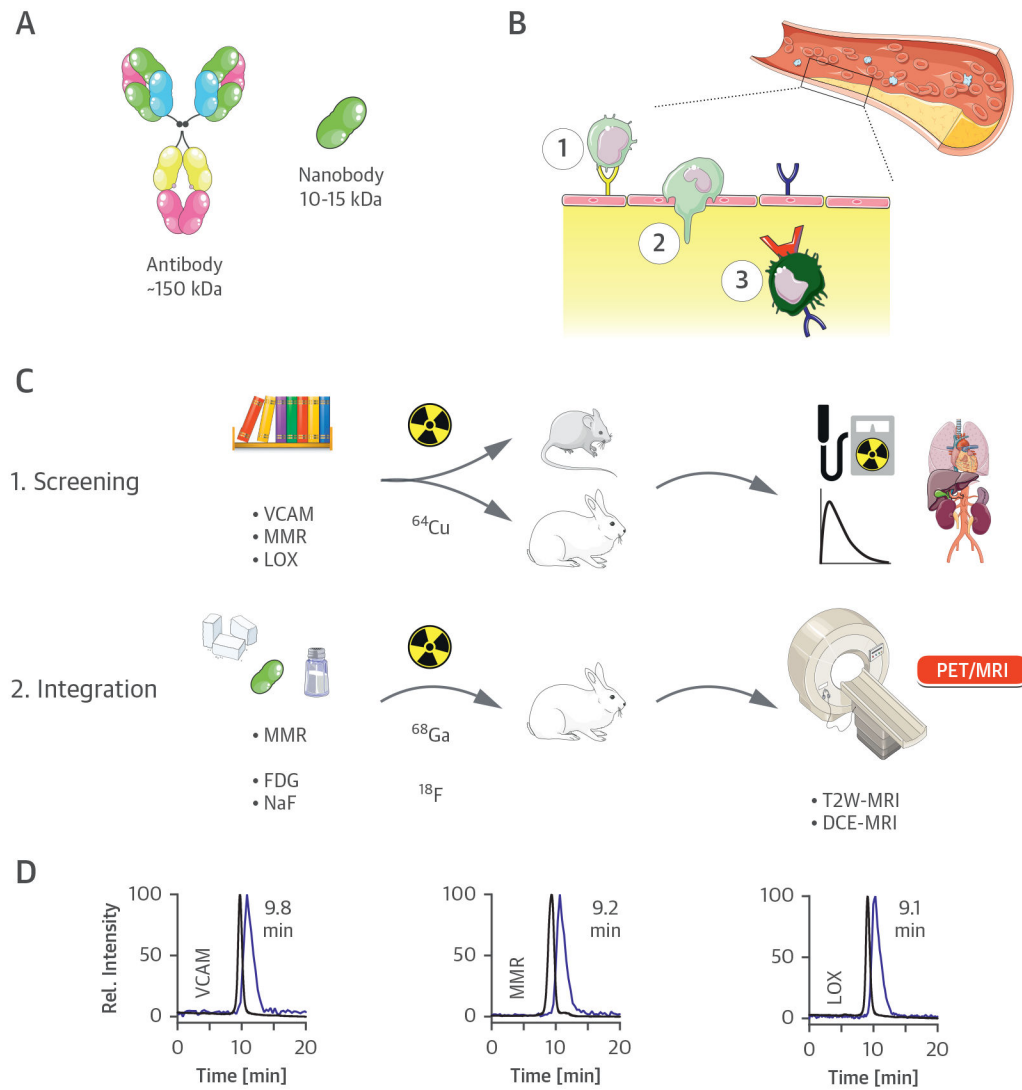
FIGURE 1. Nanobody-Facilitated Atherosclerosis PET Imaging
(A) Schematic representation of a full-size antibody and a nanobody. (B) Monocyte/
macrophage dynamics in atherosclerosis. Endothelial dysfunction is accompanied by the
expression of the surface receptor lectin-like oxidized low-density lipoprotein receptor
(LOX)-1 **(blue)** or adhesion molecules like vascular cell adhesion molecule (VCAM)-1
(yellow). Circulating monocytes are recruited to atherosclerotic lesions via interaction with
these adhesion molecules (1), leading to infiltration through the endothelium (2). Infiltrated
monocytes eventually differentiate into macrophages (3), which may also express LOX-1
and the macrophage mannose receptor (MMR) **(red)**. (C) Study outline. (D) Size exclusion
chromatograms of the 3 copper-64 (^{64}Cu) nanobodies, demonstrating coelution of
radioactivity **(blue trace)** with the nonradioactive species (black trace) ($\lambda_{abs} = 220$ nm).
DCE = dynamic contrast enhanced; ^{18}F =fluorine-18; FDG =fluorodeoxyglucose; ^{68}Ga =
gallium-68; MRI = magnetic resonance imaging; PET = positron emission tomography;
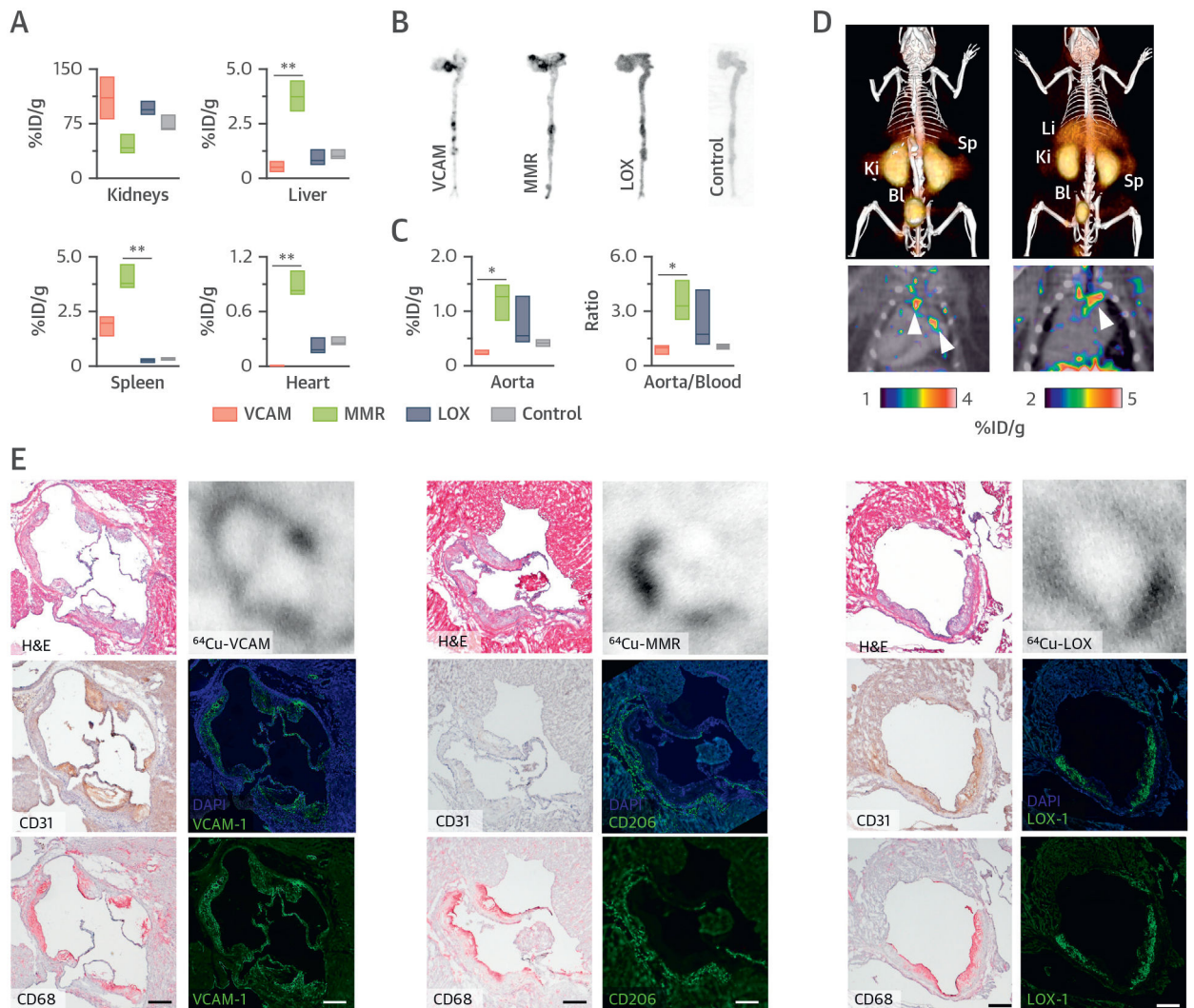T2W = T2-weighted.

FIGURE 2. Nanobody-Radiotracer Screening in Mice

(A) Radioactivity distribution in selected tissues in *Apoe*^{−/−} mice at 3 h post-injection of the corresponding ^{64}Cu-nanobody (n   3 per nanobody). Autoradiography **(B)** and radioactivity concentration **(C)** concentration in aortas of *Apoe*^{−/−} mice at 3 h post-injection of the corresponding ^{64}Cu-nanobody (n   3 per nanobody). **(D)** Representative fused PET/CT images 1 h post-injection of ^{64}Cu-VCAM **(left)** and ^{64}Cu-MMR **(right)** in *Apoe*^{−/−} mice. **Arrows** indicate enhanced uptake at the aortic arch and root, typical sites of atherosclerotic lesions. **(E)** Representative images of aortic root sections from *Apoe*^{−/−} mice with atherosclerosis showing, in the **left column**, hematoxylin and eosin (H&E) staining **(top)** and immunohistochemistry for CD31 (endothelial cells) **(middle)** and CD68 (macrophages) **(bottom)**; in the **right column**, autoradiography **(top)** and immunofluorescence for the respective targets of the 3 nanobodies with **(middle)** and without **(bottom)** 4,6-diamino-2-phenylindole (DAPI) stain. Bar = 200 μm. *p < 0.05, and **p < 0.01. %ID/g = percentage injected dose per gram of tissue; Bl = bladder; Ki = kidney; Li = liver; Sp = spleen; other abbreviations as in Figure 1.
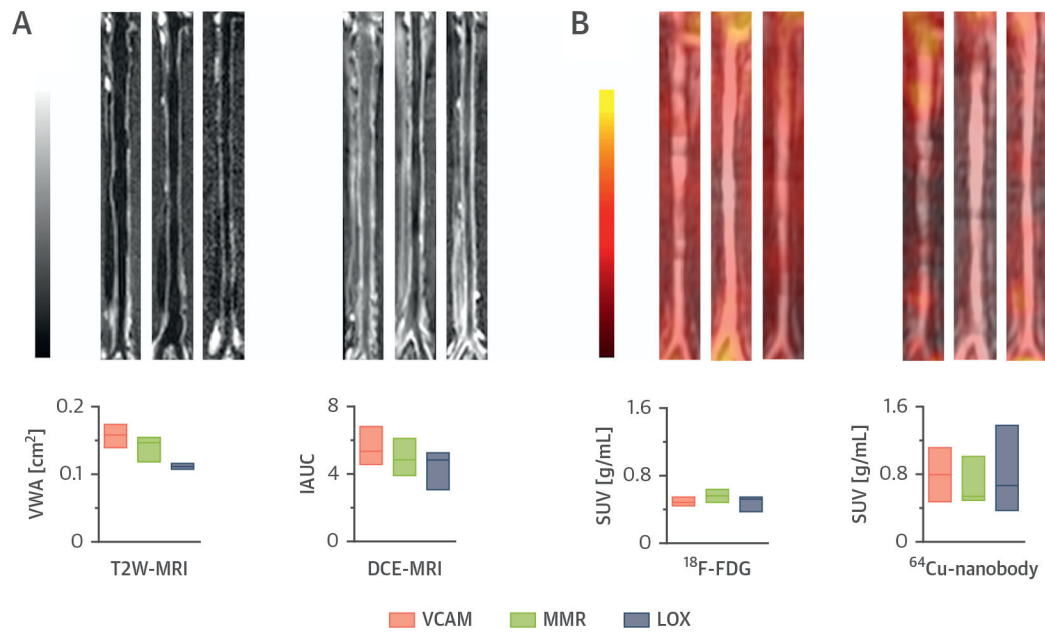
FIGURE 3. PET/MRI Plaque Phenotyping of Rabbit Atherosclerotic Aortas
(A) Representative T2W-MRI **(left)** and 3-dimensional DCE-MRI **(right)** images of aortas
from rabbits with atherosclerosis. **(B)** Representative coronal aortic PET/MR images at 3 h
post-injection (p.i.) of ^{18}F-FDG **(left)**, and at 160 min p.i. of ^{64}Cu nanobody **(right)**. In all
panels, from **left** to **right**, images are shown for the ^{64}Cu-VCAM, ^{64}Cu-MMR, and ^{64}Cu-
LOX groups. Below the images, from **left** to **right**, are shown T2WMRI vessel wall area
(VWA), DCE-MRI permeability measurements (expressed as intensity area under the curve
[IAUC] 2 min p.i. of contrast agent), and PET-derived radioactivity concentration for ^{18}F-
FDG (3 h p.i.) and ^{64}Cu-nanobodies (160 min p.i.) in abdominal aortas from rabbits with
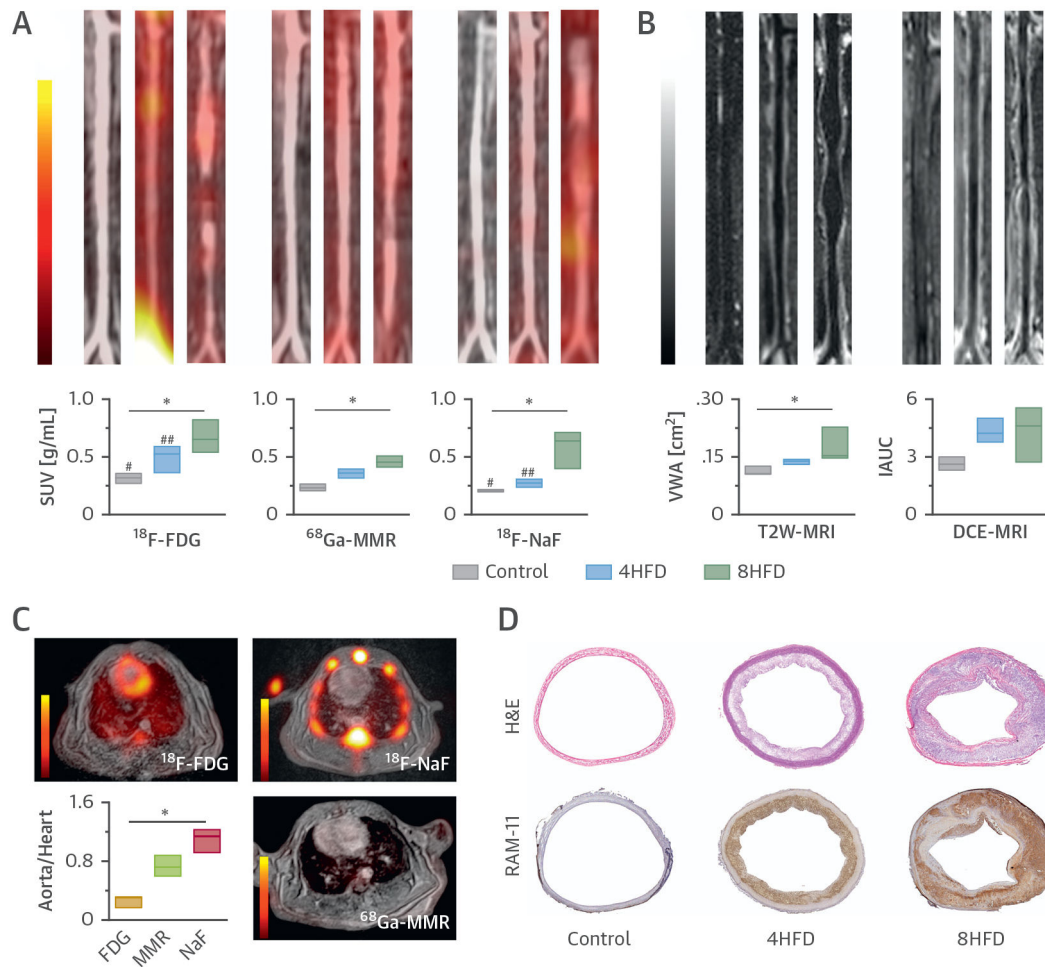atherosclerosis (n   4 per group). SUV = standardized uptake value; other abbreviations as
in Figure 1.

FIGURE 4. PET/MRI Evaluation of Atherosclerosis Progression

(A) Representative coronal aortic fused PET/MR images for ^{18}F-FDG (3 h p.i.) **(left)**, ^{68}Ga-MMR (2 h p.i.) **(middle)** and ^{18}F-NaF (1.5 h p.i.) **(right)**, and **(B)** representative T2W-MRI **(left)** and DCE-MRI **(right)** images from healthy and atherosclerotic rabbits (on high-fat diet for 4 months [4HFD] or 8 months [8HFD], n 3 per group). **(C)** Cardiac PET/MR images of the respective tracers and associated aorta-to-heart ratios in rabbits with atherosclerosis (8HFD). **(D)** Aortic sections taken from healthy control subjects and atherosclerotic rabbits (4HFD or 8HFD) and stained with H&E and RAM-11 (macrophages). *p < 0.05; ^{18}F-FDG versus ^{18}F-NaF: #p < 0.05; ##p < 0.01. Abbreviations as in Figures 1 to 3.
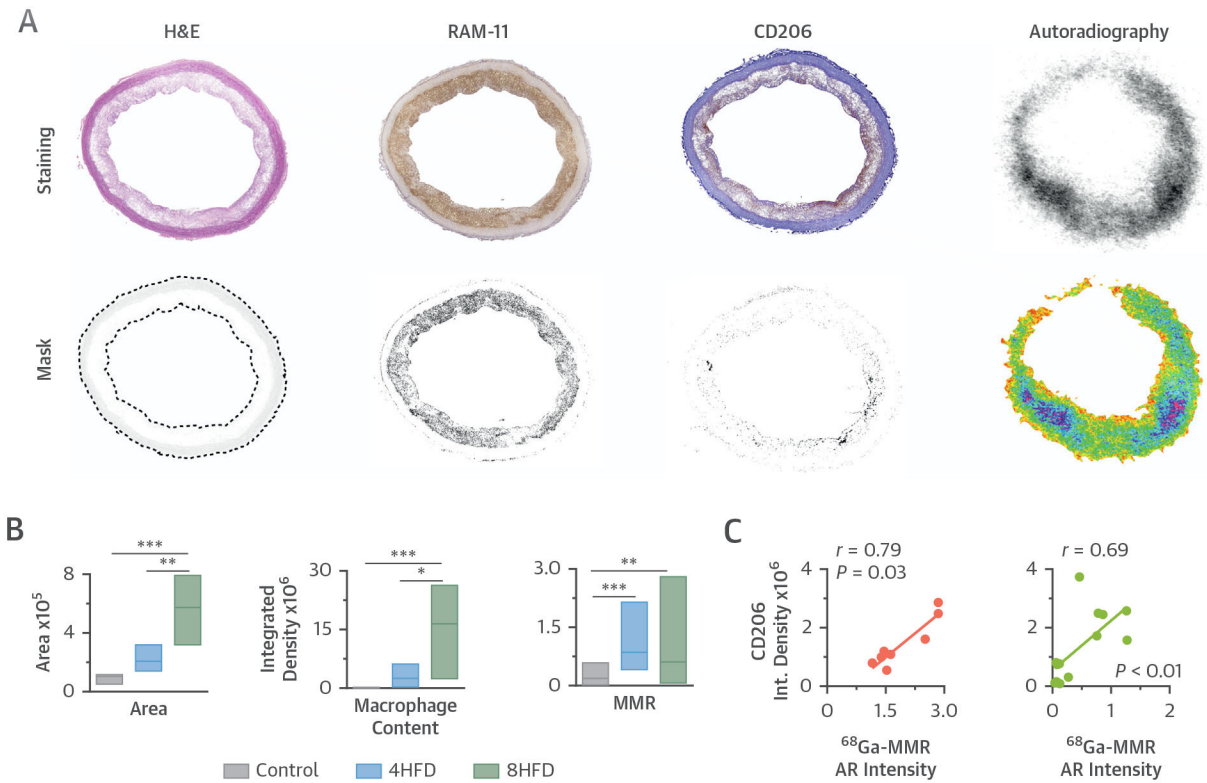
FIGURE 5. Ex Vivo Plaque Characterization
(A) Representative images of rabbit atherosclerotic aortic sections showing H&E, RAM-11 (macrophages), and CD206 (MMR-expressing macrophages) staining, and the corresponding masks. **(B)** Quantitative analysis in aortic sections, showing vessel wall area **(left)**, based on H&E staining; macrophage content **(middle)**, based on RAM-11 integrated density; and macrophage mannose expression **(right)**, based on CD206 integrated density. **(C)** Correlation between ^{68}Ga-MMR autoradiography (AR) and CD206 integrated density in aortic sections from atherosclerotic rabbits that had been 4 **(red)** and 8 months **(green)** on cholesterol-enriched high-fat diet. *p < 0.05, **p < 0.01, ***p < 0.001. Abbreviations as in Figures 1, 2, and 4.

TABLE 1

Key Features of the ^{64}Cu-Nanobody Tracers Described in this Study

	^{64}Cu-VCAM	^{64}Cu-MMR	^{64}Cu-LOX
Target	VCAM-1 (19)	MMR (21)	LOX-1 (20)
Expressed on	Endothelial cells	Macrophages	Endothelial cells and macrophages
Mouse			
Ex vivo			
Aorta-to-blood ratio	1.0 (0.6–1.1)	3.3 (2.6–4.7)	1.7 (1.3–3.6)
Aorta-to-muscle ratio	7.3 (7.3–10.3)	3.0 (2.0–9.6)	2.3 (2.2–9.8)
Rabbit			
PET			
Aorta SUV$_{max}$	0.80 (0.53–1.11)	0.54 (0.50–0.78)	0.67 (0.41–1.07)
Aorta-to-muscle ratio	6.0 (4.5–7.6)	5.5 (4.6–5.7)	5.7 (4.8–7.4)
Ex vivo			
Aorta-to-blood ratio	0.7 (0.6–1.0)	1.1 (0.8–1.3)	0.7 (0.4–1.7)
Aorta-to-muscle ratio	4.5 (4.2–5.8)	4.7 (3.1–5.4)	2.9 (2.6–3.9)
MDS-to-blood ratio	1.2 (0.8–1.7)	2.3 (1.3–2.8)	0.9 (0.4–2.2)
MDS-to-heart ratio	4.0 (3.8–5.2)	3.2 (2.7–3.8)	2.5 (2.3–3.0)

Values are median (interquartile range).

^{64}Cu = copper-64; LOX = lectin-like oxidized low-density lipoprotein receptor; MDS = most diseased segment; MMR [macrophage mannose receptor; PET = positron emission tomography; SUV [standardized uptake value; VCAM = vascular cell adhesion molecule.